Hubble Space Telescope observations of [O III] emission in nearby QSO2s: physical properties of the ionized outflows

Anna Trindade Falcão [ID],[1]★ S. B. Kraemer [ID],[1] T. C. Fischer,[2] D. M. Crenshaw,[3] M. Revalski,[2]
H. R. Schmitt,[4] M. Vestergaard,[5,6] M. Elvis,[7] C. M. Gaskell [ID],[8] F. Hamann,[9] L. C. Ho,[10] J. Hutchings,[11]
R. Mushotzky,[12] H. Netzer,[13] T. Storchi-Bergmann,[14] T. J. Turner[15] and M. J. Ward[16]

[1]*Institute for Astrophysics and Computational Sciences, Department of Physics, The Catholic University of America, Washington, DC 20064, USA*
[2]*Space Telescope Science Institute, Baltimore, MD 21218, USA*
[3]*Department of Physics and Astronomy, Georgia State University, Astronomy Offices, 25 Park Place, Suite 600, Atlanta, GA 30303, USA*
[4]*Naval Research Laboratory, Washington, DC 20375, USA*
[5]*Dark Cosmology Centre, Niels Bohr Institute, University of Copenhagen, Jagtvej 128, DK-2200 Copenhagen N, Denmark*
[6]*Steward Observatory and Department of Astronomy, University of Arizona, 933 N. Cherry Avenue, Tucson, AZ 85721, USA*
[7]*Harvard-Smithsonian Center for Astrophysics, 60 Garden Street, Cambridge, MA 02138, USA*
[8]*Department of Astronomy and Astrophysics, University of California, Santa Cruz, CA 95064, USA*
[9]*Department of Physics and Astronomy, University of California, Riverside, CA 92507, USA*
[10]*Kavli Institute for Astronomy and Astrophysics, School of Physics, Department of Astronomy, Peking University, Beijing 100871, China*
[11]*Dominion Astrophysical Observatory, NRC Herzberg Institute of Astrophysics, 5071 West Saanich Road, Victoria, BC V9E 2E7, Canada*
[12]*Department of Astronomy, University of Maryland, College Park, MD 20742, USA*
[13]*School of Physics and Astronomy, Tel Aviv University, Tel Aviv 69978, Israel*
[14]*Departamento de Astronomia, Universidade Federal do Rio Grande do Sul, IF, CP 15051, 91501-970 Porto Alegre, RS, Brazil*
[15]*Department of Physics, University of Maryland Baltimore County, 1000 Hilltop Circle, Baltimore, MD 21250, USA*
[16]*Centre for Extragalactic Astronomy, Department of Physics, University of Durham, South Road, Durham DH1 3LE, UK*

ABSTRACT

We use *Hubble Space Telescope*/Space Telescope Imaging Spectrograph long-slit G430M and G750M spectra to analyse the extended [O III] $\lambda5007$ emission in a sample of 12 nearby ($z < 0.12$) luminous ($L_{bol} > 1.6 \times 10^{45}$ erg s^{-1}) QSO2s. The purpose of the study is to determine the properties of the mass outflows of ionized gas and their role in active galactic nucleus feedback. We measure fluxes and velocities as functions of radial distances. Using CLOUDY models and ionizing luminosities derived from [O III] $\lambda5007$, we are able to estimate the densities for the emission-line gas. From these results, we derive masses of [O III]-emitting gas, mass outflow rates, kinetic energies, kinetic luminosities, momenta, and momentum flow rates as a function of radial distance for each of the targets. For the sample, masses are several times 10^3–10^7 M$_\odot$ and peak outflow rates are from 9.3×10^{-3} to 10.3 M$_\odot$ yr^{-1}. The peak kinetic luminosities are (3.4×10^{-8})–(4.9×10^{-4}) of the bolometric luminosity, which does not approach the (5.0×10^{-3})–(5.0×10^{-2}) range required by some models for efficient feedback. For Mrk 34, which has the largest kinetic luminosity of our sample, in order to produce efficient feedback there would have to be 10 times more [O III]-emitting gas than that we detected at its position of maximum kinetic luminosity. Three targets show extended [O III] emission, but compact outflow regions. This may be due to different mass profiles or different evolutionary histories.

Key words: galaxies: active – galaxies: kinematics and dynamics – galaxies: quasars.

1 INTRODUCTION

An active galactic nucleus (AGN) is a compact region at the centre of a galaxy that emits a significant amount of energy over much of the electromagnetic spectrum, and whose spectral characteristics indicate that the energy source is non-stellar. Such objects have been observed in the infrared, X-ray, radio, microwave, gamma-ray, and optical/ultraviolet (UV) wavebands.

Accreting supermassive black holes (SMBHs) are believed to be the central engines that power all AGNs. This accretion is the result of mass inflows to the central SMBH that can be triggered both from outside the galaxy, via interactions with companions, or from inside it, via secular processes (Storchi-Bergmann & Schnorr-Muller 2019). The generally adopted picture is that of a small continuum source, associated with the mass accretion flow that feeds the SMBH, surrounded by a much larger emission-line region (Osterbrock & Ferland 2006; Crenshaw et al. 2010; Kraemer et al. 2012). The extended (10–1000 s of pc) ionized gas in an AGN is referred to as the 'narrow-line region' (NLR). Here, the typical electron density is 10^2–10^6 cm^{-3} (Peterson 1997), and the gas velocity is 300–1100 km s^{-1}. The radiation released by the accretion flow to the SMBH can interact with the interstellar stellar medium of the host galaxy, ionizing and accelerating the gas. This process may regulate the

★ E-mail: anna.trindade04@gmail.com

Table 1. Column 4 lists the distance to the QSO2, considering a Hubble constant $= 71$ km s^{-1} Mpc^{-1}. Column 5 lists the maximum radial extent of the AGN-driven outflows, with emission lines, which exhibit high centroid velocities and/or multiple emission lines with multiple components. Column 6 lists the maximum radial extent of the disturbed gas, with low centroid velocities and FWHM > 250 km s^{-1} (F18). Column 7 lists the δr for each target.

Target	Redshift	Scale (kpc arcsec^{-1})	Distance to QSO2 (Mpc)	Deproj. R_{out} (kpc)	Deproj. R_{dis} (kpc)	δr (pc)
(1)	(2)	(3)	(4)	(5)	(6)	(7)
SDSS J115245.66+101623.8	0.070	1.30	296	0.15	1.23	0.71
MRK 477	0.038	0.72	161	0.54	0.90	0.03
MRK 34	0.051	0.95	215	1.89	1.89	0.06
2MASX J17135038+5729546	0.113	1.97	477	0.65	>0.92	0.13
2MASX J16531506+2349431	0.103	1.83	435	0.57	1.16	0.14
2MASX J14054117+4026326	0.081	1.47	342	0.33	>0.94	0.08
2MASX J13003807+5454367	0.088	1.59	372	0.16	0.16	0.08
2MASX J11001238+0846157	0.101	1.80	427	0.69	>1.51	0.14
2MASX J08025293+2552551	0.081	1.48	342	0.57	0.89	0.09
2MASX J07594101+5050245	0.054	1.02	228	0.67	0.67	0.05
FIRST J120041.4+314745	0.116	2.04	490	1.07	>1.59	0.10
B2 1435+30	0.092	1.66	389	0.20	>1.74	0.09

SMBH accretion rate. The relationship between the SMBH mass and the stellar velocity dispersion of its galaxy bulge (Kormendy & Ho 2013, and references therein) is credited to the action of the AGN quenching star formation and evacuating gas from the bulge, a process referred to as 'AGN feedback' (Begelman 2004).

Various physical scenarios for effective feedback have been suggested. These include quenching star formation through negative feedback (Wylezalek & Zakamska 2016), triggering star formation through positive feedback (Silk 2013; Mahoro, Povic & Nkundabakura 2017), or more complex interactions (Zubovas & Bourne 2017).

AGN feedback certainly exists in radio-loud AGNs, whose powerful jets are highly collimated, but they occur in only 5–10 per cent of the AGN population (Rafter, Crenshaw & Wiita 2009). Meanwhile, winds are prevalent in most AGNs (Mullaney et al. 2013; Genzel et al. 2014; Woo et al. 2016). AGN winds are frequently observed as UV and X-ray absorption lines blueshifted with respect to their host galaxies, originating in gas within tens to hundreds of parsec from the central SMBH (Crenshaw, Kraemer & George 2003; Veilleux, Cecil & Bland-Hawthorn 2005; Crenshaw & Kraemer 2012; King & Pounds 2015), or emission-line gas in AGN NLRs (Crenshaw & Kraemer 2005; Crenshaw et al. 2010; Müller-Sánchez et al. 2011; Fischer et al. 2013, 2014; Bae & Woo 2016; Nevin et al. 2016). Recent studies (e.g. Fischer et al. 2018, hereafter F2018) question how effective AGN feedback is on galactic-bulge scales, as required in a star formation quenching, negative feedback scenario. Therefore, it is important to quantify its impact, which can be accomplished by characterizing the physical properties of these outflows, such as mass, velocity, mass outflow rate, and kinetic energy.

While previous studies suggested that the power of the outflows scales with luminosity (Ganguly & Brotherton 2008), some ground-based studies of QSO2s (Greene et al. 2011; Liu et al. 2013; Harrison et al. 2014; McElroy et al. 2015) have found that powerful and very extended outflows detected by the optical [O III] λ5007 emission line are extremely rare. This raises the question of whether kpc-scale AGN winds exist in most QSO2s. The answer to this question can be decisive on the matter of whether outflows are a critical component of quasars feedback and hence the evolution of galaxy bulges, or if the star formation is quenched in bulges by other means.

F2018 obtained *Hubble Space Telescope* (*HST*) imaging and spectroscopy of 12 of the 15 most luminous targets at $z \leq 0.12$ from the Reyes et al. (2008) sample of QSO2s, through Hubble Program ID 13728 (PI: Kraemer) and archival observations of Mrk 34 (see Table 1). They measured [O III] velocities and line profile widths as a function of radial distance in order to characterize mass outflows in these QSO2s.

In regard to the morphology of the sample, F2018 found that in some of the targets the [O III] region is very extended, such as in FIRST J120041.4+314745, which has a maximum radial extent in its [O III] image, R_{max}, of 5.92 kpc. Meanwhile, other targets present a very compact morphology, such as 2MASX J14054117+4026326 that possesses an $R_{max} = 0.88$ kpc.

Regarding the kinematics of the ionized gas, F2018 showed that the extent of the outflows, R_{out}, in most of the sample, is relatively small compared to the overall extent of the [O III] emission region, R_{max}, with an average $R_{out}/R_{max} = 0.22$, except for Mrk 34, for which $R_{out}/R_{max} \sim 1$ (see Table 1). They found that one can categorize the influence of the central AGNs in different regions, as a function of distance from the nucleus. In the inner region, the emission lines have multiple components and include velocity profiles that differ from rotation, i.e. with high central velocities and high full width at half-maximum (FWHM), and hence are consistent with outflows. At greater distances, gas is still being ionized by the AGN radiation but emission lines exhibit low central velocities with a low FWHM, consistent with rotation of the host galaxy. In addition, F2018 identified a third kinematic component, namely gas with low central velocities, but high FWHM. They refer to this as 'disturbed' kinematics and suggested that AGN activity may be disrupting gas without resulting in radial acceleration.

Previous work (Fischer et al. 2017; Wylezalek & Morganti 2018) explored the idea that the outflows are radiatively accelerated, although we see in our targets a rotational component as well. At large distances, this is consistent with the fact that the flux of radiation is low, but the gravitational deceleration due to the enclosed stellar mass is large; therefore, the gas cannot be radially accelerated. However, at smaller distances, the rotation component may simply be gas that has not been exposed to the AGN radiation long enough to be accelerated.

In this study, we use the same data as F2018, and we extend their analysis by computing masses, mass outflow rates, kinetic energies, kinetic energy rates, momenta, and momentum flow rates for the same sample of QSO2s. Throughout this paper, we adopt a flat

Lambda cold dark matter cosmology with $H_0 = 71 \, \mathrm{km \, s^{-1} \, Mpc^{-1}}$, $\Omega_0 = 0.28$, and $\Omega_\lambda = 0.72$.

2 SAMPLE, OBSERVATIONS, AND MEASUREMENTS

2.1 *HST* observations

We use medium dispersion spectra[1] to characterize the physical properties and kinematics of the emission-line gas, along with [O III] imaging to determine the ionized gas mass. As already discussed in F2018, the observing program for our sample was performed in a two-step process: First, we obtained narrow-band images of each AGN to determine ideal Space Telescope Imaging Spectrograph (STIS) position angles (PAs) and, later, a spectroscopic observation. To obtain the images for our sample, the FR505N or FR551N filters were used, chosen depending on the redshift of each target to observe [O III], with the Wide-Field Channel of *HST*/Advanced Camera for Surveys (ACS). The FR647M filter was used to obtain the continuum observations.

The long-slit spectra used in this study were obtained with STIS using either the G430M or G750M gratings to study the [O III] kinematics, employing a 52 arcsec × 0.2 arcsec slit oriented along the major axis of the NLR.

2.2 Spectral fitting

We fit the emission line in each row (i.e. in the spatial direction) of the STIS spectral image with Gaussians in order to obtain the [O III] velocities, relative to systemic, and fluxes. We employ a Bayesian fitting routine, discussed by Fischer et al. (2017), that uses the Importance Nested Sampling algorithm in the MultiNest library (Feroz & Hobson 2008; Feroz, Hobson & Bridges 2009; Feroz et al. 2013; Buchner et al. 2014) to compute the logarithm of the evidence, $\ln(Z)$, for each model, as shown in Fig. 1.

The models are run for zero Gaussian components, i.e. no [O III] emission, and then for one Gaussian component. If the one-component model is chosen over the zero-component model,[2] the data are analysed with a two-component model, and the process is repeated until the more complex model ($\ln Z_{n+1}$) is no longer chosen over the previous one ($\ln Z_n$). The uncertainty in flux for each line is calculated from the residuals between the data and the fit. However, the flux uncertainties are small compared to those discussed in Section 2.4.

2.3 [O III] image analysis

In order to account for the mass of [O III]-emitting gas outside of the area sampled by the STIS slit, we use a continuum-subtracted [O III]-emission-line image of the entire NLR for each target. The flux calibration included scaling by the filter bandpass. These correction factors are equal to 2 per cent of the linear ramp filter wavelength, or approximately 100 Å, for each image (Ryon 2019).

Our measurements and velocities discussed in Section 2.2 are deprojected according to the analysis of the Sloan Digital Sky Survey (SDSS) images, as described in F2018. An example of the [O III] image and azimuthally summed flux profile are shown in Fig. 2, for

---

[1] $R = \lambda/\Delta\lambda \sim 5000–10\,000$ (Woodgate et al. 1998).

[2] The one-component model has to have a significantly better evidence value, $|\ln \frac{Z_1}{Z_0} > 5|$, in order to be chosen over the zero-component model.
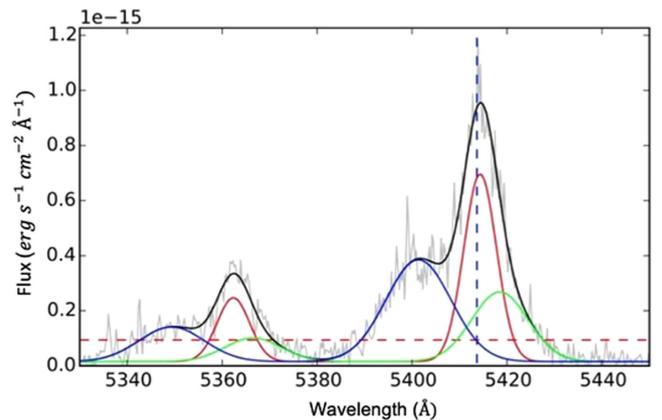
Figure 1. [O III] $\lambda\lambda 4959$, 5007 emission-line component fitting example over the continuum peak in 2MASX J08025293+2552551. The continuum peak refers to the brightest row in the 2D CCD data, where, if one takes a vertical, 1D cut along the image (avoiding the emission lines), that row would be the peak of the flux distribution. [O III] $\lambda 4959$ fit parameters are fixed to be identical to [O III] $\lambda 5007$ fit parameters, with line flux fixed to be 1/3 of [O III] $\lambda 5007$ flux. Grey line represents STIS spectral data. Solid black line represents the total model. Red, blue, and cyan lines represent individual Gaussians. Vertical dashed blue line represents the [O III] $\lambda 5007$ wavelength at systemic velocity. Horizontal dashed red line represents the 3σ continuum-flux lower limit for Gaussians in our fitting. Figure from F18.
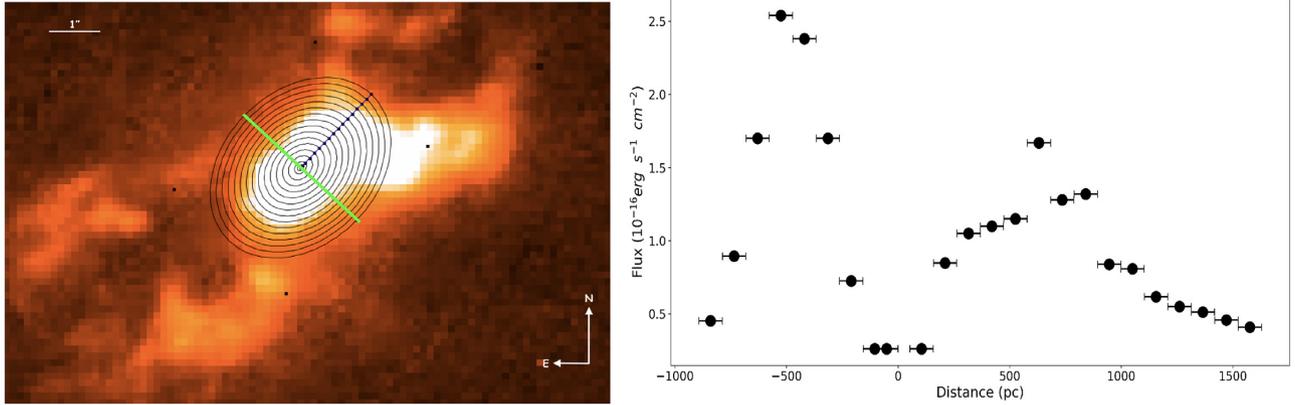
FIRST J120041.4+314745.

To determine the total [O III] flux as a function of distance from the nucleus, we use the Elliptical Panda routine, in the SAOImage DS9 Software (Joye & Mandel 2003). Following F2018 (see sections 2.5 and 3.1 of F2018), we assume that the host galaxies are disc galaxies and that the inclination of their discs to our line of sight can be obtained from the ellipticities of their isophotes. The ellipticities and PAs of our targets are given in table 2 of F2018 along with the PAs of the ionization comes. Following Fischer et al. (2017) and F2018, we furthermore assume that most of the AGN-ionized gas structure in type 2 AGNs lies in their host discs, and that we can thus use the host disc orientation assumed for each galaxy to deproject *HST* measurements for our QSO2 sample to determine true physical distances in the plane of the host galaxy. Annuli of constant distance from the centres of the galaxies are ellipses with their major axes in the PA as given in table 2 of F2018. We add up the [O III] flux in a series of elliptical annuli of radius δr (see Table 1), where δr is the deprojected length along the slit for each extraction. These annuli are illustrated for one of our targets in the left-hand panel of Fig. 2. We divide each elliptical annulus in two with one half for each side of the ionization cone.

2.4 Constraints on luminosity

In type 2 AGNs, the inner region, nearest to the SMBH, is hidden from view (Antonucci 1993); therefore, one has to use indirect indicators to estimate the bolometric luminosity, except in cases where the X-ray absorber is not Compton thick. One method is to use the total [O III] luminosity, $L_{[O III]}$, and a bolometric correction factor (e.g. Heckman et al. 2004), but there is some uncertainty in the value of the factor depending on the extinction (Lamastra et al. 2009) and the Eddington ratio (Duras et al. 2020).

In order to estimate the extinction towards the NLRs of the QSO2s, we retrieved the fluxes of Hα and Hβ from SDSS (Ahumada et al. 2019). The observed ratios of Hα/Hβ range from 4.7, for 2MASX

Figure 2. The left-hand panel shows the *HST* [O III] image of FIRST J120041.4+314745 with superimposed elliptical semi-annuli representing rings of constant distance from the nucleus. The green line represents the positions where we divide the two semi-ellipses. The orthogonal black line represents the direction of the slit. The right-hand panel is the [O III] annulus fluxes oriented along the major axis of the ellipse. The negative values are to the south-east and the positive values are to the north-west. Ellipses very close to the nucleus have a very small size, leading to low fluxes in the centre positions. Fluxes at positions >900 pc (to the south-east side) are too low to be detected. The radial axes in the right-hand panel are asymmetric because the kinematic fits were limited to this range.

Table 2. Column 2 lists the corrected [O III] luminosity, as discussed in Section 2.4. All targets have $L_{\text{[O III]}} \geq 1.9 \times 10^{42}$, satisfying the conventional *B*-band absolute magnitude criterion of a 'quasar', $B_{\text{mag}} < -23$, where a corresponding $L_{\text{[O III]}}$ is $> 3 \times 10^8$ $L_{\odot}$ (Zakamska 2003). Column 3 lists the corrected bolometric luminosity for each QSO2, calculated as described in Section 2.4. Column 4 lists the corrected number of ionizing photons per second. Column 5 lists the ratio between the retrieved fluxes of Hα and Hβ from SDSS for each target. Column 6 lists the degree of reddening for each target in our sample, calculated using the values for Hα and Hβ from their SDSS spectra. Due to the similar redshifts and selection criteria, the range in luminosities is small (by a factor of ~4).

Target	$L_{\text{[O III]}}$ (erg s^{-1})	L_{bol} (erg s^{-1})	Q (photons s^{-1})	Hα/Hβ	$E(B-V)$
(1)	(2)	(3)	(4)	(5)	(6)
SDSS J115245.66+101623.8	3.5×10^{42}	1.6×10^{45}	4.8×10^{54}	3.68	0.19
MRK 477	4.0×10^{42}	1.8×10^{45}	5.4×10^{54}	3.76	0.21
MRK 34	5.7×10^{42}	2.6×10^{45}	7.8×10^{54}	3.98	0.26
2MASX J17135038+5729546	6.1×10^{42}	2.8×10^{45}	8.3×10^{54}	3.65	0.18
2MASX J16531506+2349431	1.1×10^{43}	4.9×10^{45}	1.5×10^{55}	4.40	0.35
2MASX J14054117+4026326	4.6×10^{42}	2.1×10^{45}	6.2×10^{54}	4.00	0.26
2MASX J13003807+5454367	4.8×10^{42}	2.2×10^{45}	6.5×10^{54}	3.54	0.15
2MASX J11001238+0846157	8.5×10^{42}	3.9×10^{45}	1.2×10^{55}	3.60	0.17
2MASX J08025293+2552551	8.0×10^{42}	3.6×10^{45}	1.1×10^{55}	4.59	0.39
2MASX J07594101+5050245	8.6×10^{42}	3.9×10^{45}	1.2×10^{55}	4.70	0.41
FIRST J120041.4+314745	1.3×10^{43}	5.8×10^{45}	1.7×10^{55}	3.52	0.15
B2 1435+30	7.1×10^{42}	3.2×10^{45}	9.6×10^{54}	4.33	0.33

J07594101+5050245, to 3.5, for FIRST J120041.4+314745. In AGNs, the intrinsic ratio can range from the theoretical ratio 2.9 (Osterbrock & Ferland 2006) to ~3.1, for broad-line decrements (Dong et al. 2008). Since our sample consists of QSO2s, we are only detecting Balmer lines from the NLR; therefore, to calculate the reddening, we assume an intrinsic ratio of 3.0. Taking into account this intrinsic ratio and the Galactic extinction curve (Savage & Mathis 1979),[3] we calculate the reddening, $E(B-V)$, for all the targets in our sample. We assume that the same reddening applies to the entire [O III]-emitting regions for each target in our sample. Note that the extinction occurs in dust along our line of sight, both within the Galaxy and the individual QSOs. The results are listed in Table 2.

To calculate the values for the bolometric luminosity, L_{bol}, for our targets, we correct the values of $L_{\text{[O III]}}$ as described in Seaton (1979), using the reddening listed in Table 2. Then, we calculate L_{bol} using the corrected $L_{\text{[O III]}}$ and the bolometric correction factor from Lamastra et al. (2009), which is 454 for the range in luminosities in our sample.[4] Our results are listed in Table 2.

For the entire spectral energy distribution (SED), we assume that it can be fitted using a number of broken power laws of the form

$$L_{\nu} \propto \nu^{-\alpha}, \tag{1}$$

[3]Using the extinction curve of Cardelli, Clayton & Mathis (1989) results in a less than 4 per cent change in the computed reddening, compared to the curve of Savage & Mathis (1979).

[4]There are other ways to calculate the bolometric luminosity using the combined [O III]+[O I] or Hβ and [O III], as described in Netzer (2009). Based on the SSD spectra, using these methods, we obtain $L_{\text{bol}} = 1.4 \times 10^{45}$ erg s^{-1} for Mrk 34, which is in reasonable agreement with what we obtain using the corrected [O III] and the Lamastra correction for this target.

where α, the spectral or energy index, is a positive number (e.g. Laor et al. 1997; Meléndez et al. 2011). We assume that the UV to lower energy, 'soft' X-ray, is characterized by one value of α, while the higher energy, 'hard' X-ray, has a lower value of α. For our study, we adopt a cut-off at 100 keV and we set the breakpoint at 500 eV, using the following values (Revalski et al. 2018):

$$\alpha = 1.0 \text{ for } h\nu < 13.6 \text{ eV};$$

$$\alpha = 1.4 \text{ for } 13.6 \text{ eV} \leq h\nu \leq 500 \text{ eV};$$

$$\alpha = 1.0 \text{ for } 500 \text{ eV} \leq h\nu \leq 10 \text{ keV};$$

$$\alpha = 0.5 \text{ for } 10 \text{ keV} \leq h\nu \leq 100 \text{ keV}.$$

It is likely that the 'soft' X-ray continuum is more complex than what we assume (e.g. Kraemer et al. 2002; Netzer et al. 2002). However, we opt to use the same SED as in Revalski et al. (2018) to allow for a direct comparison of the results for Mrk 34.

The number of ionizing photons per second emitted by the AGN, based on this SED, is

$$Q = C_2 \int_{13.6\,\text{eV}}^{500\,\text{eV}} \left(\frac{\nu^{-1.4}}{h\nu}\right) \mathrm{d}\nu + C_1 \int_{500\,\text{eV}}^{10\,\text{keV}} \left(\frac{\nu^{-1.0}}{h\nu}\right) \mathrm{d}\nu$$
$$+ C \int_{10\,\text{keV}}^{100\,\text{keV}} \left(\frac{\nu^{-0.5}}{h\nu}\right) \mathrm{d}\nu, \qquad (2)$$

where h is the Planck constant.

Specifically for Mrk 34, Gandhi et al. (2014) were able to determine the X-ray luminosity, $L_{(2-10\,\text{keV})} = 9(\pm3) \times 10^{43}$ erg s^{-1}, which makes it possible to calculate Q for this target. They did not detect any significant variability between their *NuSTAR* and *XMM–Newton* observations. Therefore, we do not consider the possible variability of the X-ray source. The constants C, C_1, and C_2 were determined by normalizing to the $L_{(2-10\,\text{keV})}$.

We then use the corrected $L_{[O\,III]}$ for Mrk 34 to get the ratio $Q/L_{[O\,III]}$, which we apply to all the other QSO2s. Our results are presented in Table 2.

In order to estimate the uncertainties introduced by our SED, we recalculate Q for $1.0 \leq \alpha \leq 1.8$, over the range from 13.6 to 500 eV. This results in a factor of 3 change compared to the value of Q computed for $\alpha = 1.4$. Other sources of uncertainty include those of: the X-ray luminosity, which Gandhi et al. assumed to be $\sim$30 per cent; the uncertainty in the ratio Hα/Hβ, $\sim$15 per cent; a factor of 2 in our assumed ionization parameter; the deprojected positions, $\sim$10 per cent; and a factor of 2 uncertainty in the correction for the bolometric luminosity (Lamastra et al. 2009). Adding all these in quadrature results in an uncertainty of a factor of $\sim$4, which applies to the hydrogen density determination (see Section 2.5).

We can also compare the value for L_{bol} for Mrk 34 derived from the corrected [O III] with the value computed from our model SED. The latter method consists of extending the SED down to 1 eV and, using $\alpha = 1.0$ from 1 to 13.6 eV, calculating the bolometric luminosity by integrating over the continuum. The value we get for L_{bol} from our SED is $\sim$58 per cent of the [O III] derived value. The difference could be due to our assumed SED or the reddening correction applied to the [O III] emission. However, the difference is less than the uncertainties in Q discussed in the previous paragraph.
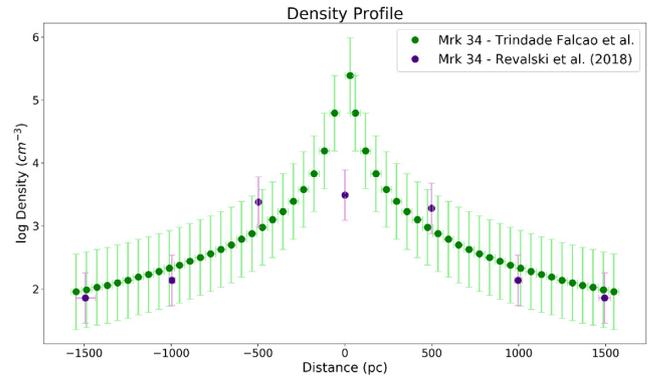
Figure 3. A comparison between the gas densities obtained applying our photoionization models (in green) and the gas densities obtained by Revalski et al. (2018) (in purple) for Mrk 34. The points in purple are the densities for Revalski et al.'s medium component. Their point at the centre sums up a region $\sim$10 times larger than the region we are sampling. Therefore, their density is an average over the sampled region, hence much lower than our computed value.

2.5 Photoionization models and constraints on gas density

To convert observed [O III] fluxes in a slit element into masses of gas at that position, we need to know the volume of emitting gas and its density. This is conventionally done by using density-sensitive line ratios such as the [S II] and [O II] doublet ratios. Since we only have observations of [O III] (and Hβ for three of the targets in our sample, as discussed in Section 2.4), we estimate the density from the dimensionless ionization parameter, U, where

$$U = \frac{Q}{4\pi r^2 n_H c}, \qquad (3)$$

where r is the radial distance from the AGN, n_H is the hydrogen number density (see Section 2.4), and c is the speed of light. We compute the values of $Q(H)$ for all the QSO2s in the sample, as shown in Table 2.

Revalski et al. (2018) used a multicomponent photoionization model for Mrk 34. Based on the model parameters and results given in their tables 6 and 7, the 'medium' component, for which they assumed $\log(U) = -2$, accounts for most of the [O III] emission. Also, this component contains almost all the mass at each of the points modelled by them, except for two positions, where the ionization is dominated by a higher ionization component. This results in their determination of higher densities for the [O III] component, as shown in Fig. 3. Therefore, we model the [O III]-emission-line gas, at each radial position, with a single component of $\log(U) = -2$. This means that the density drops with r^{-2}, for the [O III] gas along the whole emitting region (as also proposed by Davies et al. 2020).

We use version 17.00 of CLOUDY (Ferland et al. 2017) to construct photoionization models with $\log(U) = -2$. These predict $\frac{[O\,III]}{H\beta} \geq 10$, which we confirmed for the targets with both [O III] and Hβ based on measurements of the STIS spectra (2MASX J07594101+5050245, 2MASX J11001238+0846157, and 2MASX J16531506+2349431, which have an average $\frac{[O\,III]}{H\beta} = 10.2$).

In dusty gas, emission lines are suppressed by two mechanisms. One is the dust absorption of multiply scattered resonance lines, such as Lyα (e.g. Kraemer & Harrington 1986). The other is due to the depletion of elements, such as Si, Mg, and Fe on to dust grains. STIS long-slit UV spectra of the NLR typically show fairly strong Mg II λ2800 (Kraemer et al. 2000, 2001; Collins et al. 2005), which suggests that the refractory elements are not heavily depleted. While

these spectra reveal a wide range of Ly α/H β ratios, they generally range from 10 to 20, which indicates the presence of some dust within the emission-line gas. Based on these studies, we assume a dust-to-gas ratio of 50 per cent that of the Galactic interstellar medium with proportional depletion of elements from gas phase, consistent with Revalski et al. (2018). This dust is not the source of the line-of-sight reddening discussed in Section 2.4.

While supersolar abundances appear to be common in broad-line region gas, at least in QSOs (e.g. Hamann & Ferland 1998; Dietrich et al. 2003), NLR studies indicate abundances closer to solar (Nagao, Murayama & Taniguchi 2001; Nagao et al. 2002). Based on their photoionization analysis of the NLR, Groves, Dopita & Sutherland (2004) argued for a N/H ratio approximately twice solar, consistent with other NLR studies (e.g. Storchi-Bergmann, Rodríguez-Ardila & Schmitt 1996; Kraemer, Ruiz & Crenshaw 1998; Storchi-Bergmann et al. 1998). Since N/H increases as $(Z/Z_{solar})^2$ (Talbot & Arnett 1973), where Z is the fractional abundance of heavy elements, this ratio corresponds to elemental abundances of approximately 1.4× solar, which we adopt for this study.

The exact logarithmic values relative to hydrogen by number are: C $= -3.54$, N $= -3.88$, O $= -3.205$, Ne $= -3.92$, Na $= -5.61$, Mg $= -4.47$, Al $= -5.70$, Si $= -4.64$, P $= -6.44$, S $= -4.73$, Ar $= -5.45$, Ca $= -5.81$, Fe $= -4.65$, and Ni $= -5.93$. In order to account for the grain composition, we include depletions from gas phase for C, O and the refractory elements (e.g. Snow & Witt 1996). Note that dust can play an important role in the dynamics of outflows (e.g. Baron & Netzer 2019). We will be examining the outflow dynamics in our subsequent paper (Trindade Falcão et al., in preparation).

For reference, we calculate the maximum possible column density of the gas emitting [O III]. This is when the gas is radiation bounded. Specifically, the modelling integration stopped when the electron temperature drops below 4000 K, at which point the ionizing radiation has essentially been exhausted. It is possible that the total column densities are greater than this, but we have no means of detecting that gas in these data. On the other hand, it is quite likely that the gas is not radiation bounded in places. What matters is the volume of gas emitting [O III]. We calculate this in the next section.

As shown in Fig. 3, this method does a reasonable job in matching densities from detailed photoionization models. We then use the computed column densities, N_H, to calculate the masses and, subsequently, the other physical properties of the [O III] gas, as described in Section 4.

3 CALCULATIONS

To determine the various quantities associated with the outflow as a function of distance from the SMBH, we first need to determine the mass of gas in each of our semi-annuli. We do this by first estimating M_{slit}, the mass of gas inside the *HST* STIS slit at a given radius, and then scaling this to the mass in the whole semi-annulus by multiplying the ratio of the total [O III] flux in the semi-annulus, $F_{[O III]ann}$, to the flux in the slit, $F_{[O III]m}$. For our calculations, we only consider points lying inside the range of outflow defined in F2018.

The mass of gas emitting [O III], in grams, in each position along the slit is giving by (Crenshaw et al. 2015)

$$M_{slit}(r) = N_H \mu m_p \left(\frac{L_{[O III]}}{F_{[O III]c}} \right), \tag{4}$$

where N_H is the hydrogen column density, assumed to be the same as the column density modelled by CLOUDY, μ is the mean mass

per proton,[5] and m_p is the mass of a proton. To get the mass of gas, the column density needs to be multiplied by an effective area. The term in parentheses gives the effective surface area of the emitting gas as seen by the observer. $F_{[O III]c}$ is the [O III] luminosity per cm^2 calculated by CLOUDY and $L_{[O III]}$ is the observed luminosity calculated from the reddening corrected flux in the slit. That is,

$$L_{[O III]} = 4\pi D^2 F_{[O III]m}, \tag{5}$$

where D is the distance to the QSO2s (see Table 1) and $F_{[O III]m}$ is the intrinsic flux measure at each point in the STIS spectra.

Physically, the equation for M_{slit} (equation 4) determines the area of the emitting clouds through the ratio of the luminosity and flux, and then multiplies this by the column density to yield the total number of particles, which, when multiplied by the mean mass per particle, gives the total ionized mass.

We estimate the mass of gas in the half-annulus at a given radial distance from the centre by scaling the mass in the slit (equation 4) by the ratio of the flux in the entire semi-annulus to the flux in the slit.

Specifically, the total ionized mass in outflow at each radial distance is

$$M_{out}(r) = M_{slit}(r) \left(\frac{F_{[O III]ann}}{F_{[O III]m}} \right), \tag{6}$$

where $F_{[O III]ann}$ is the flux in each half image annulus of width δr, as shown in Fig. 2. Thus, our method assumes that throughout the semi-annulus the gas has the same density, N_H, and outflow velocity, v_{out}, as the gas at the slit location.

After calculating $M_{out}(r)$, we are able to estimate the mass outflow rates [$\dot{M}_{out}(r)$], kinetic energies (E), kinetic luminosities ($\dot{E}$), momenta (p), and momentum flow rates ($\dot{p}$). All these quantities are related to the power and impact of the NLR outflows (King & Pounds 2015).

The mass outflow rates [$\dot{M}_{out}(r)$] are calculated, at each point along the NLR, using

$$\dot{M}_{out}(r) = \frac{M_{out}(r)v_{out}}{\delta r}, \tag{7}$$

where v_{out} is the deprojected outflow velocity at the distance of the semi-annulus; the deprojection factors are the same as those used in F2018 (see Section 2.3).

The kinetic energies (in erg), kinetic luminosities (in erg s^{-1}), momenta (in dyne-s), and momentum flow rates (in dyne)[6] are given by

$$E(r) = \frac{1}{2} M_{out} v_{out}^2 \tag{8}$$

$$\dot{E}(r) = \frac{1}{2} \dot{M}_{out} v_{out}^2 \tag{9}$$

$$p(r) = M_{out} v_{out} \tag{10}$$

$$\dot{p}(r) = \dot{M}_{out} v_{out}. \tag{11}$$

The momenta and momentum flow rates can be compared to the AGN bolometric luminosity, and the radiation pressure force, $\frac{L}{c}$, to quantify the efficiency of the NLR in converting radiation from the AGN into the radial motion of the outflows (Zubovas & King 2012; Costa, Sijacki & Haehnelt 2014).

---

[5]We use $\mu = 1.4$, which is consistent with roughly solar abundances.
[6]1 dyne = 1 g cm s^{-2} = 10^{-5} N.
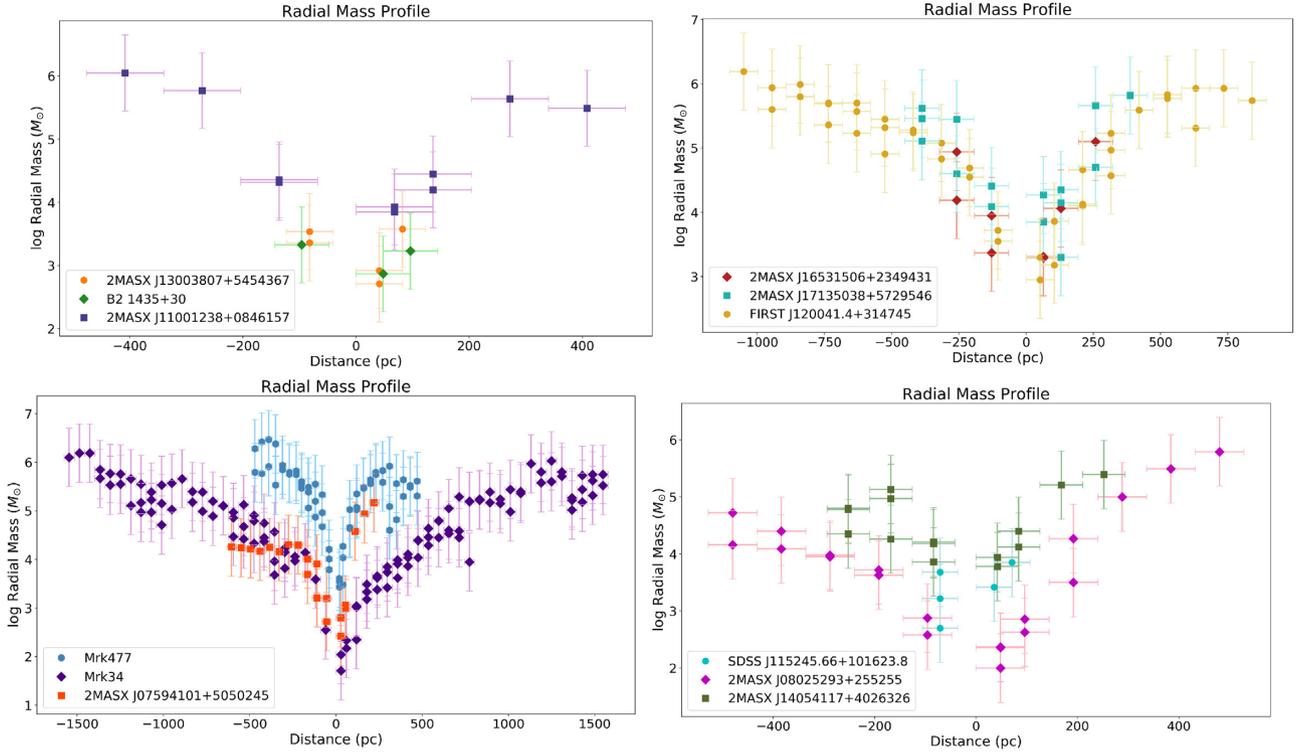
Figure 4. Ionized mass profile in units of $M_\odot$ calculated from the total flux in each semi-elliptical annulus for all the targets in our sample. QSO2s with similar redshifts were plotted together. All points considered in the plots are inside the range of outflow defined in F2018. With a few exceptions, most mass profiles look similar. So the total outflow mass is primarily determined by where the outflow stops and the rotation kinematics begin. Each annulus has a $\delta r = 0.05$ arcsec, and, due to the range in distances of our targets, δr corresponds to a range of physical lengths in pc.

All the uncertainties discussed in Section 2.4, which affect our determination of the hydrogen density, result in corresponding uncertainty in our mass calculations. Hence, the quantities computed in equations (7)–(11) have the same factors of uncertainty.

4 RESULTS

We present our mass profiles, outflow rates, and other kinematic properties as functions of distance from the SMBH in Figs 4–9. The quantities shown are the values within each bin of length δr. Table 3 gives the total masses outflowing and the maxima of the kinematic properties. Table 4 gives the radii of the peaks in these quantities.

Among the QSO2s in our sample, the outflow has a maximum radial extent that extends from 130 to 1600 pc from the nucleus and contains a total ionized gas mass ranging from $4.6^{+13.8}_{-3.45} \times 10^3$ to $3.4^{+10.2}_{-2.55} \times 10^7 \, M_\odot$, in the outflow region (Fig. 4). The kinematics at further distances are consistent with disturbance and rotation, but not with outflows, as discussed in F2018.

For all targets in our sample, the total ionized mass at the innermost points is low (see Fig. 4), which can be explained by the fact that the dense gas in this region radiates more efficiently (see Osterbrock & Ferland 2006), leading to smaller masses being required to produce the same observed [O III] emission. Additionally, the area sampled in the annuli is an increasing function of radius, meaning that less mass is added from the images at smaller distances.

The peak in the mass outflow rate peaks from $9.3^{+27.9}_{-7.0} \times 10^{-3} \, M_\odot$ yr^{-1}, for B2 1435+30, to $10.3^{+30.9}_{-7.7} \, M_\odot \, \mathrm{yr}^{-1}$, for Mrk 34 (Fig. 5), at a distance varying from 100 to 1260 pc from the nucleus (see Table 4) and then decreases at larger distances.

The maximum kinetic energy for the targets extends from $8.2^{+24.6}_{-6.1} \times 10^{50}$ erg, for SDSS J115245.66+101623.8, to $2.6^{+7.8}_{-1.9} \times 10^{54}$ erg, for Mrk 34. The total kinetic luminosity ranges from $3.5^{+10.5}_{-2.6} \times 10^{-8}$ of L_{bol}, for SDSS J115245.66+101623.8, to $4.1^{+12.3}_{-3.1} \times 10^{-3}$ of L_{bol}, for Mrk 34.

The radiation pressure force from the bolometric luminosity, $\frac{L_{\mathrm{bol}}}{c}$, ranges from $5.4^{+16.2}_{-4.0} \times 10^{34}$ dyne, for SDSS J115245.66+101623.8, to $1.9^{+5.7}_{-1.4} \times 10^{35}$ dyne, for FIRST J120041.4+314745. The peak momentum flow rate extends from $7.5^{+22.5}_{-5.6} \times 10^{30}$ dyne, for SDSS J115245.66+101623.8, to $2.8^{+8.4}_{-2.1} \times 10^{34}$ dyne, for Mrk 34. Thus, considering the maximum momentum flow rate among our sample, the peak outflow momentum rate is ∼30 per cent of the AGN's radiation pressure force, although it is a much smaller percentage for most of our sample.

The quantities displayed are the value contained within each bin of width δr. In addition, we neglect contributions to the mass outflow rates and energetics from the significant FWHM of the emission lines, which could be due, for example, to the ablation of gas off the spiral dust lanes.

5 DISCUSSION

The maximum kinetic luminosities of the outflow for our sample are presented in Table 3 and are $(3.4^{+10.2}_{-2.5} \times 10^{-8})$–$(4.9^{+14.7}_{-3.7} \times 10^{-4})$ of the AGN bolometric luminosities. This does not approach the (5.0×10^{-3})–(5.0×10^{-2}) range used in models of efficient feedback (Di Matteo, Springel & Hernquist 2005; Hopkins & Elvis 2010). The low ratios of $\dot{E}/L_{\mathrm{bol}}$ were also found in other samples by Baron & Netzer (2019) and Davies et al. (2020); however, these are much less
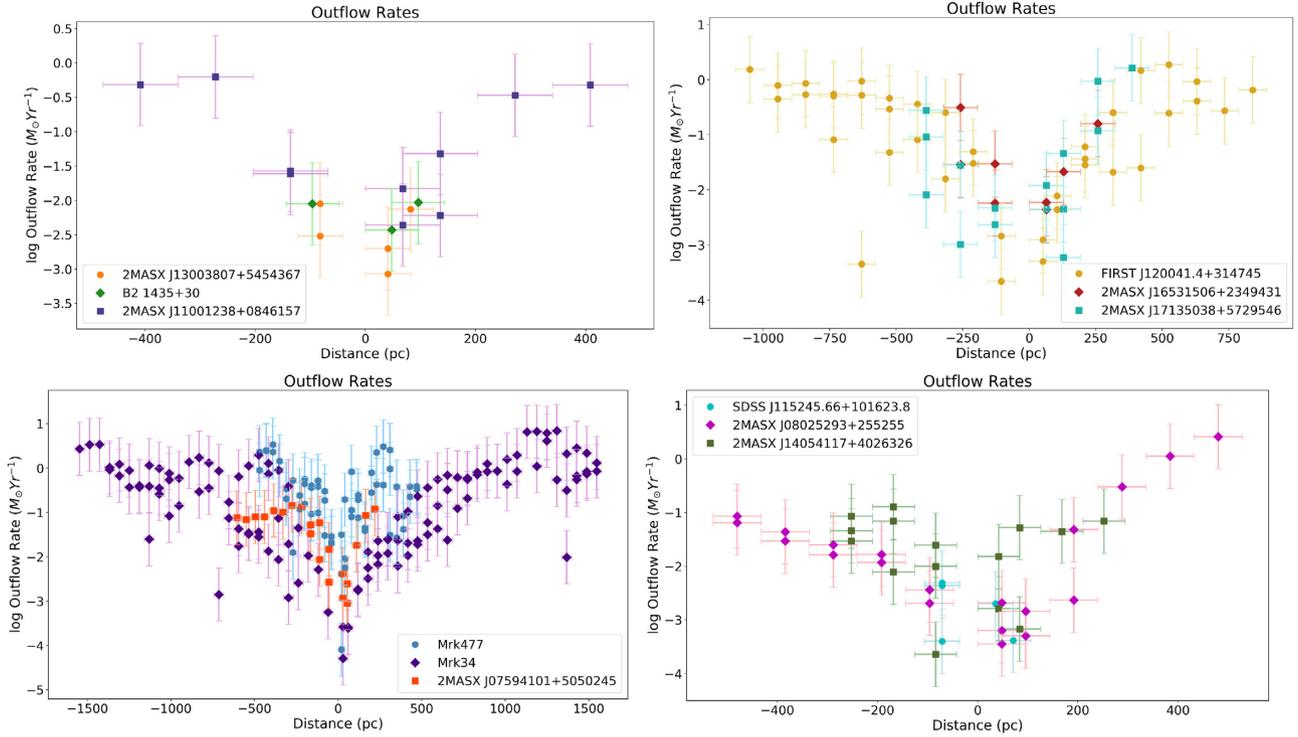
Figure 5. Spatially resolved outflow rates for all targets, assuming that all of the material is in outflow. Same as Fig. 4.
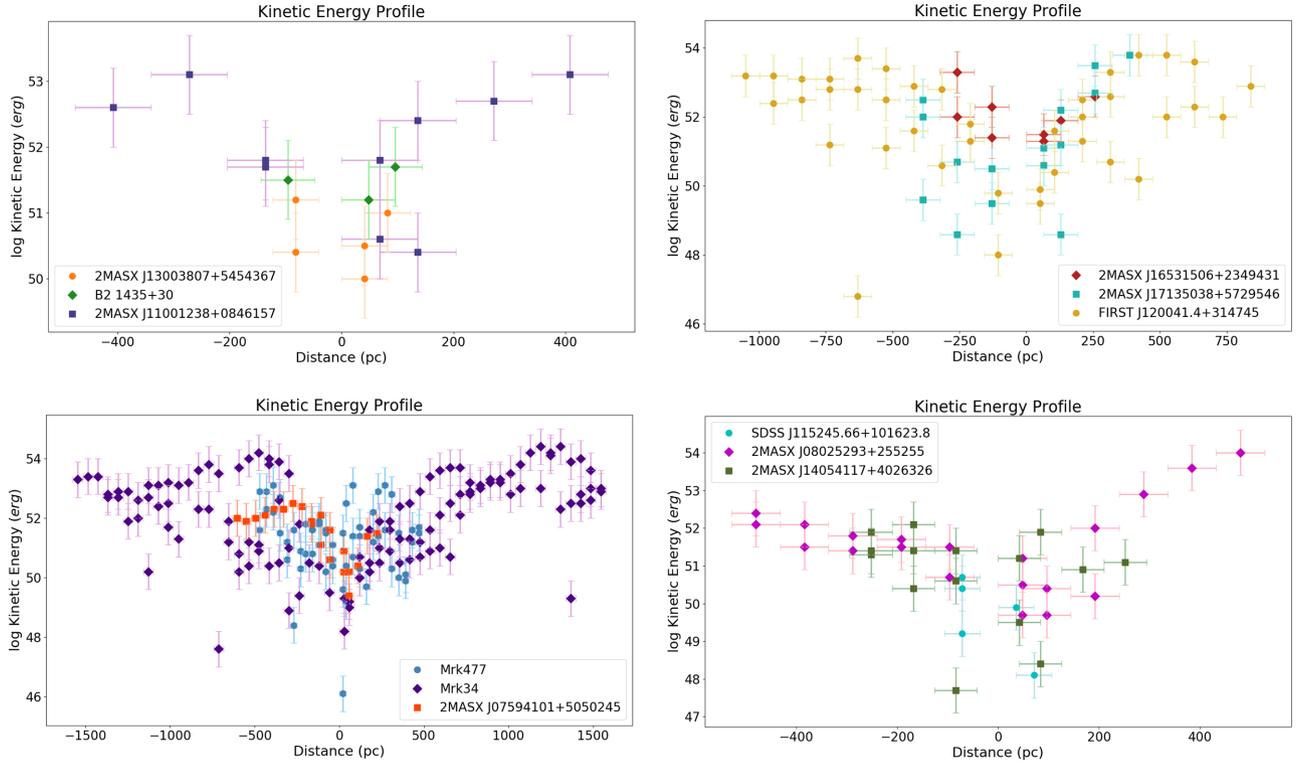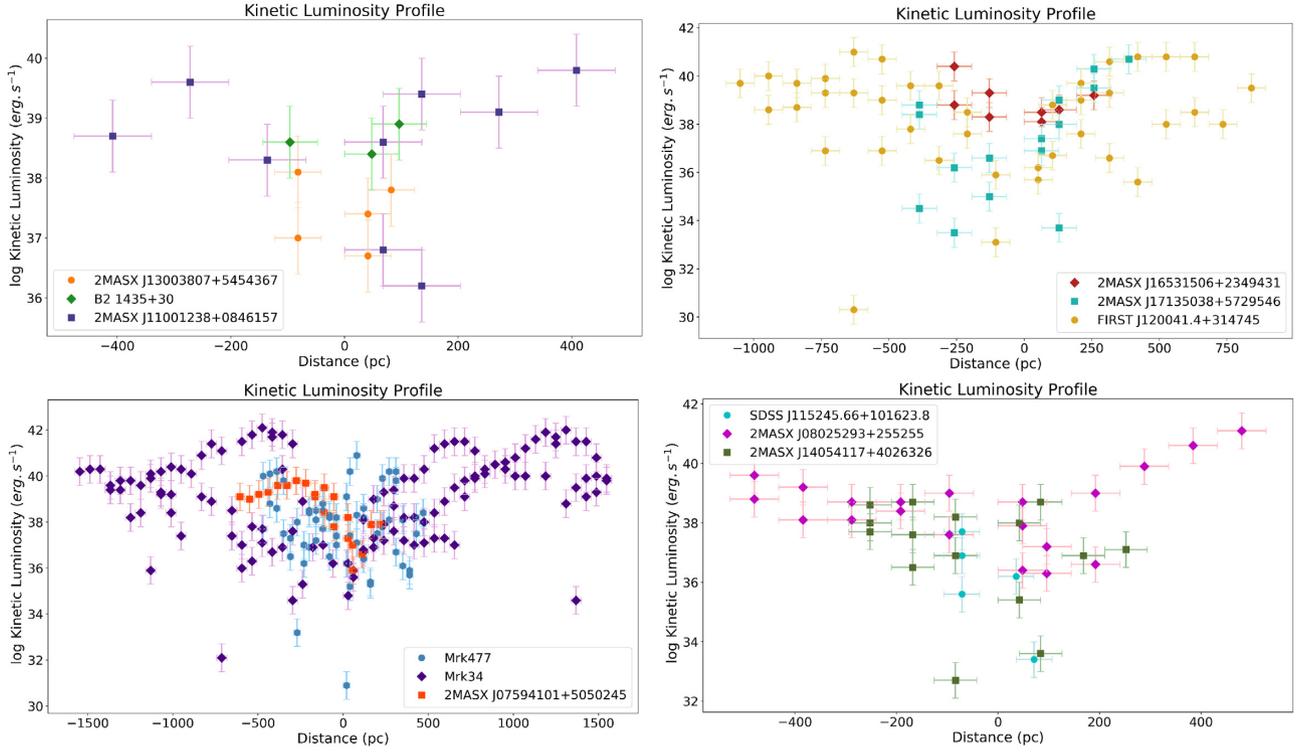

Figure 6. Kinetic Energy profiles for all targets. See Section 4.

than those derived from relativistic outflows (UFOs) observed in the X-ray spectra of some AGNs (Bischetti et al. 2019).

We also study the relation between the maximum outflow rate for each target and the position where the maximum outflow rate occurs (Fig. 10, right-hand panel), as well as the relation between the maximum outflow rate and R_{out} for each target in our sample (Fig. 10, left-hand panel). For a majority of the targets, the maximum outflow rate appears to be correlated with R_{out}, since the further away the gas

Figure 7. Kinetic luminosity rates calculated for all targets. QSO2s with similar redshifts were plotted together. See Section 4.
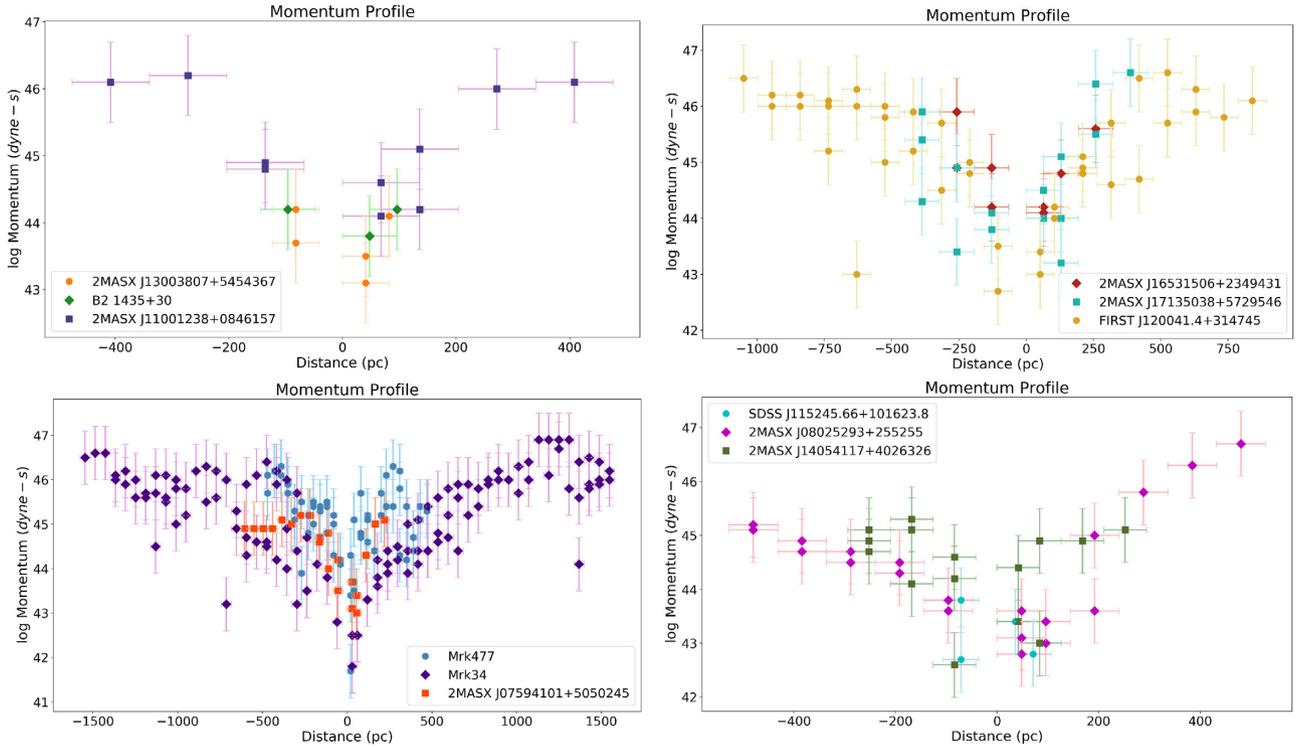
Figure 8. Momentum profiles for all targets. See Section 4.

is from the SMBH, the larger the amount of gas is needed to produce the same amount of ionized gas mass, as the density drops.

After concluding that these QSO2s do not produce effective feedback, based on models previously discussed, we calculate how much mass an outflow would have to have to produce a $\dot{E} =$ 0.5 per cent of L_{bol}, which is considered to be the value where feedback effects could be relevant[7] (Hopkins & Elvis 2010).

---

[7]The maximum $\dot{E}$ does not necessarily occur at the point where the target has its maximum outflow rate, since $\dot{E} \sim v_{out}^3$.
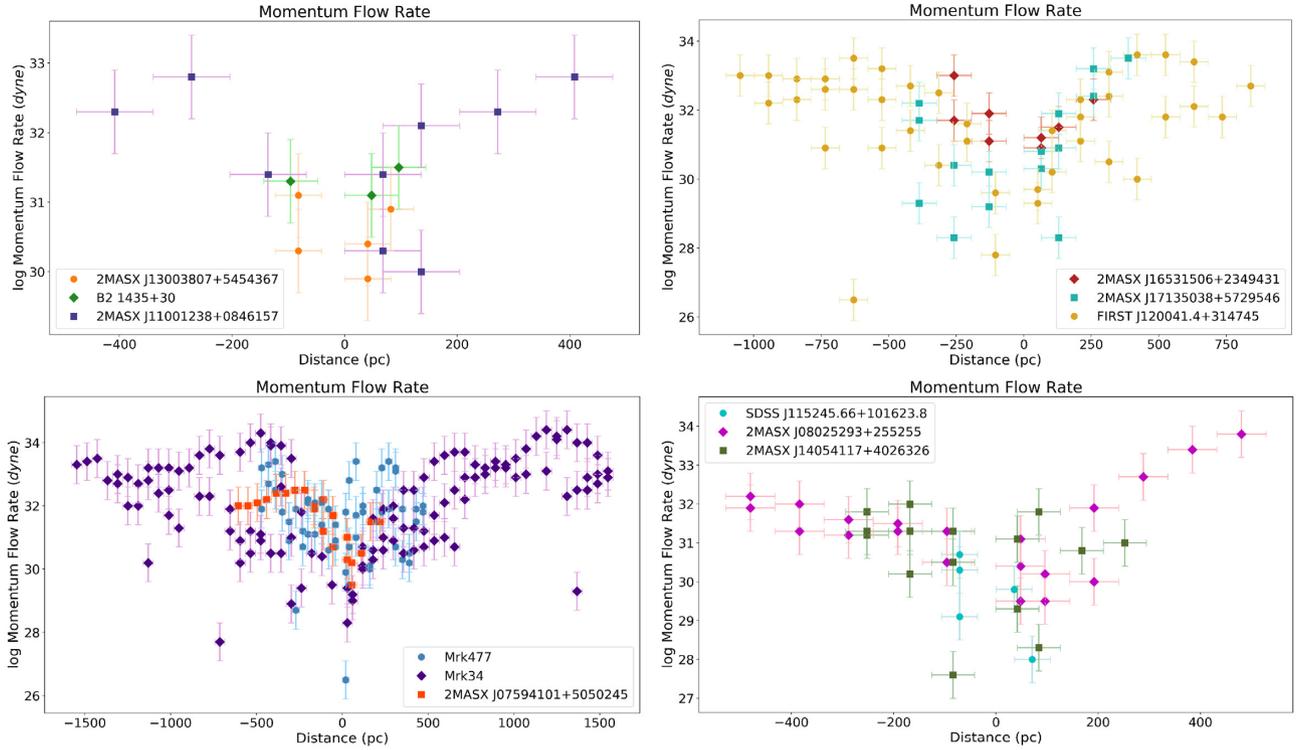
Figure 9. Momentum flow rates. See Section 4.

Table 3. Numerical results for the mass and energetic quantities for the outflowing gas component in each target of our sample. All results account for the gas within the outflow region. Column 2 is the gas mass in units of $10^5 \, M_\odot$, column 3 is peak mass outflow rate within the outflow region, column 4 is the peak kinetic energy, column 5 is the peak kinetic luminosity, column 6 is the peak momentum, and column 7 is the peak momentum flow rate for each QSO2. All listed values have a factor of ~ 4 uncertainty, as discussed in Section 2.4.

Target	Total mass ($10^5 \, M_\odot$)	Maximum $\dot{M}$ ($M_\odot \, yr^{-1}$)	Maximum E (10^{53} erg)	Maximum $\dot{E}$ (10^{41} erg s^{-1})	Maximum p (10^{46} dyne s)	Maximum $\dot{p}$ (10^{34} dyne)
(1)	(2)	(3)	(4)	(5)	(6)	(7)
SDSS J115245.66+101623.8	0.17	0.01	<0.01	<0.01	0.01	<0.01
MRK 477	152.0	3.55	1.34	0.75	2.09	0.3
MRK 34	337.0	10.3	26.20	12.80	9.15	2.83
2MASX J17135038+5729546	24.40	1.64	6.50	0.51	4.17	0.33
2MASX J16531506+2349431	2.54	0.34	2.23	0.25	0.95	0.10
2MASX J14054117+4026326	8.94	0.20	0.14	<0.01	0.34	0.01
2MASX J13003807+5454367	0.11	0.01	0.02	<0.01	0.02	<0.01
2MASX J11001238+0846157	25.60	0.63	1.32	0.07	1.68	0.06
2MASX J08025293+2552551	11.80	2.58	9.54	1.27	4.86	0.64
2MASX J07594101+5050245	4.44	0.14	0.29	0.07	0.15	0.03
FIRST J120041.4+314745	140.0	2.11	6.34	1.00	4.35	0.39
B2 1435+30	0.04	<0.01	0.45	<0.01	0.02	<0.01

We calculate the required mass for Mrk 34, at its point of maximum $\dot{E}$, using the highest deprojected outflow velocity component calculated using the fitting routine by Fischer et al. (2017) for that same position, $v_{out} = 1.4 \times 10^3$ km s^{-1}. We choose Mrk 34 since, among the targets in our sample, it is the target that shows the highest outflow rate and most extended outflows. We find that, in order to reach the lower limit of $\dot{E}/L_{bol} = 0.5$ per cent, Mrk 34 would have to possess an outflow rate of $20 \, M_\odot \, yr^{-1}$, in contrast to our measured value of $1.97^{+5.9}_{-1.5} \, M_\odot \, yr^{-1}$. This corresponds to a mass, at that position, of $M_{0.5 \, per \, cent} = 8.2 \times 10^5 \, M_\odot$, as opposed to our measured value of $8.1^{+24.3}_{-6.1} \times 10^4 \, M_\odot$.

We also calculate the maximum amount of mass, M_{max}, that Mrk 34 could have at this distance, i.e. the maximum amount of gas that

could be at this distance if the entire solid angle around the SMBH were covered. Specifically,

$$M_{max}(r) = 4\pi r^2 (\mu m_p N_H), \qquad (12)$$

where r is the deprojected radial distance. We are assuming that the gas is distributed in a complete shell at this distance. We find that the maximum amount of mass that Mrk 34 could possess at this position is $M_{max}(r) = 1.3 \times 10^8 \, M_\odot$, which is greater than the value for $M_{0.5 \, per \, cent}$. However, only a small fraction of that mass is emitting [O III] radiation.

If we consider the position where Mrk 34 has its peak outflow rate, 1.26 kpc, in order to calculate how much mass it would need to

Table 4. Deprojected distance from the nucleus for peak measurements of mass outflow rates (column 2), kinetic luminosities (column 3), and momentum flow rates (column 4). Column 5 lists the highest deprojected outflow velocity at the maximum outflow rate position.

Target	Position of peak $\dot{M}$ (pc)	Position of peak $\dot{E}$ (pc)	Position of Peak $\dot{p}$ (pc)	v_{out} at peak $\dot{M}$ (km s^{-1})
(1)	(2)	(3)	(4)	(5)
SDSS J115245.66+101623.8	70	70	70	70.9
MRK 477	310	80	310	22.9
MRK 34	1260	480	1320	341
2MASX J17135038+5729546	390	390	390	312
2MASX J16531506+2349431	260	260	260	498
2MASX J14054117+4026326	170	170	170	42.4
2MASX J13003807+5454367	50	50	50	206
2MASX J11001238+0846157	270	410	410	144
2MASX J08025293+2552551	480	480	480	393
2MASX J07594101+5050245	275	275	275	379
FIRST J120041.4+314745	525	840	525	325
B2 1435+30	100	100	100	518
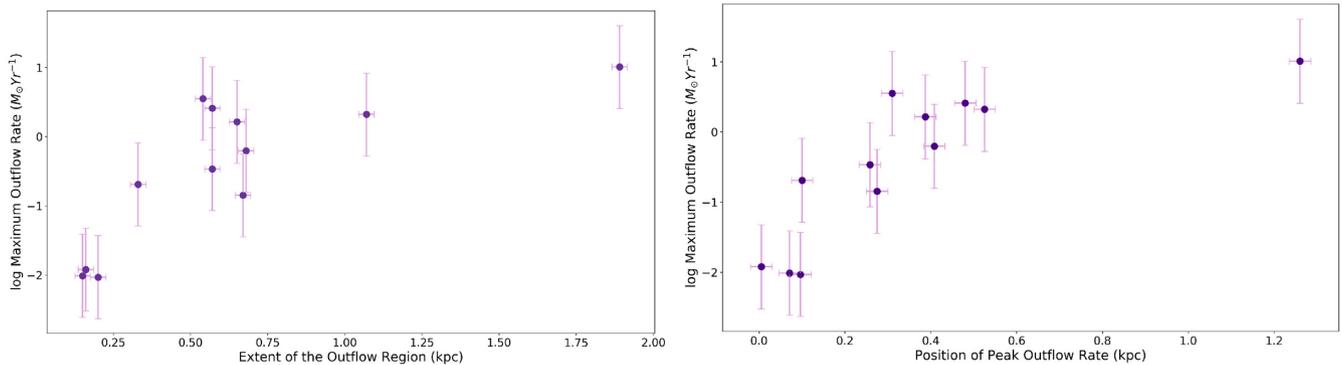
Figure 10. For a majority of our sample, it is possible to see a relation between the maximum outflow rate and R_{out} (left-hand panel) and the position where the peak outflow rate occurs and the maximum outflow rate for each target (right-hand panel).

reach 0.5 per cent of its bolometric luminosity, and using the highest deprojected outflow velocity at that position, $v_{out} = 6.1 \times 10^2$ km s^{-1}, we find that there would need to be an outflow rate of 109 M$_\odot$ yr^{-1}, in contrast to our measured value of $4.1^{+12.3}_{-3.1}$ M$_\odot$ yr^{-1} (in Revalski et al. 2018, the peak outflow rate occurs at ∼0.5 kpc, where the deprojected outflow velocity is ∼2000 km s^{-1}, which would require an outflow rate of ∼40 M$_\odot$ yr^{-1}). This corresponds to a mass, at that position, of 1.0×10^7 M$_\odot$, as opposed to our measured value of $4.0^{+12.0}_{-3.0} \times 10^5$ M$_\odot$. We find that the maximum amount of mass that Mrk 34 could possess at this position is $M_{max}(r) = 7.4 \times 10^8$ M$_\odot$, which is also greater than the value for $M_{0.5\,per\,cent}$.

These results tell us that the required amount of gas for efficient feedback is less than what we would estimate for a covering factor of unity, which means that it is theoretically possible to have an $\dot{E}$ = 0.5 per cent of L_{bol}. One explanation for the low values we are obtaining for the mass outflow rate is that the source of the outflow, e.g. cold molecular and possibly atomic gas in the disc (Fischer et al. 2017), has a very low covering factor compared to a sphere at its location.

Another possibility is that the gas does not remain in the state in which it emits [O III] for long. If it is not confined by an external medium, e.g. a lane of gas and dust in the host disc, it will rapidly thermally expand. As it does so, the density drops, and the ionization state of the gas increases to the point where it becomes X-ray emission-line gas (as suggested by Kraemer et al. 2020). In this case, the outflows could be dominated by the X-ray-emitting gas.

We will be exploring this scenario in a future paper (Trindade Falcão et al., in preparation).

Another characteristic of these targets is the relation between the total ionized mass and the maximum outflow rate for each AGN.

We plot these quantities in two different ways:

1) considering the total ionized mass only within the outflow range (Fig. 11, left-hand panel);

2) considering the ionized mass including the mass outside the outflow range (Fig. 11, right-hand panel).

When comparing the two plots, we find that three AGNs, namely SDSS J115245.66+101623.8, 2MASX J13003807+5454367, and B2 1435+30, are separate from the remainder of the QSO2 sample. Their shift in positions from the left-hand panel to the right-hand panel on Fig. 11 is due to their very extended [O III] emission, based on the ACS images, despite having very weak outflow rates.

To better understand the conditions under which the gas can be efficiently accelerated, we can use the velocity calculation for radiatively driven outflows, discussed by Das, Crenshaw & Kraemer 2007, where

$$v(r) = \sqrt{\int_{r_1}^{r} A_1 L_{bol} \frac{\mathcal{M}}{r^2} - A_2 \frac{M(r)}{r^2} \, dr}, \qquad (13)$$

where $\mathcal{M}$ is the Force Multiplier, i.e. the ratio of the total absorption cross-section to the Thomson cross-section, and $M(r)$ is the enclosed mass at the distance r, determined from the radial mass distribution
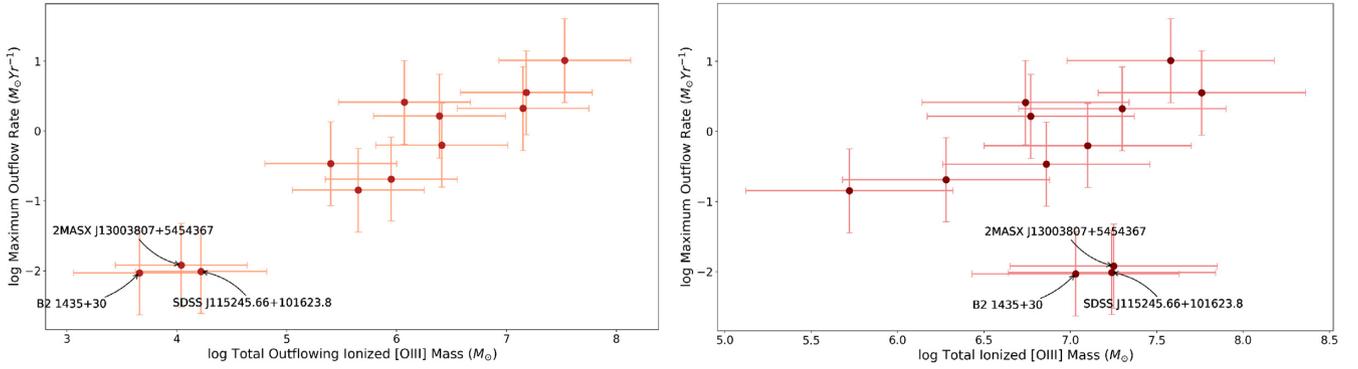
Figure 11. The left-hand panel shows the relation between the maximum outflow rate for each target and the total ionized mass in the outflow range. The right-hand panel shows the relation between the maximum outflow rate for each target and the total ionized mass including the regions outside the outflow range.

of the host galaxy, including the bulge. The constants A_1 and A_2 are given in Das et al. (2007).

Taking into account the relevant parameters in equation (13), specifically, L_{bol} and $M(r)$, there are two possibilities that can explain the distinct characteristics of these three QSO2s:

1) The AGN was in a low state until recently. We can rule out the possibility that it was 'off' completely by estimating the recombination times for the [O III] gas, as follows:

$$\tau = \frac{1}{n_H \alpha_{rec}}. \tag{14}$$

The total recombination rate for O^{++}–O^+ is $\alpha_{rec} = 2.52 \times 10^{-12}$ cm^3 s^{-1}, at 10^4 K (Nahar 1999). Based on our model densities, the recombination times (equation 14) are relatively short (the minimum recombination times are ∼3–4 yr and the maximum range from 245 to 370 yr); therefore, it is possible that the AGN could have turned completely off. However, even if the AGN was on, it appears to be in too weak of a state to accelerate the [O III] gas at these distances.

If the AGN was in a weak state, it could have enough ionizing radiation to produce [O III]. However, the L_{bol} would have been too low, up to recently, to accelerate the gas, that it would not be able to accelerate the gas, since the first term in equation (13) becomes smaller compared to the gravitational deceleration term.

If we assume that the existence of outflows close to the AGN means that the AGN is back to a high state, we can estimate how long ago it entered into this high state by using the size of the outflow regions and calculating the light crossing time for each target. Our calculations show that for SDSS J115245.66+101623.8, 2MASX J13003807+5454367, and B2 1435+30, these values are ∼230, 270, and 310 yr ago, respectively.

2) The AGN has not varied in luminosity, but the three targets have different mass distributions than the other QSO2s in our sample. This possibility can be considered as two distinct cases:

a) The bulge mass is more centrally peaked. If this is the case, the second term in equation (13) starts to dominate closer to the nucleus. However, the velocities and outflow rates for these three targets are similar to those of the rest of the sample in the same distance range (see Table 4). This suggests that this scenario is unlikely.

b) These objects possess a mass component that starts to dominate some distance from the AGN, as in Mrk 573 (see Fischer et al. 2017, fig. 14). In this case, outflows can be generated close to the AGN, but, when this outer component starts to dominate, the gas cannot be accelerated. However, in order to explore this possibility, we would

need deeper (higher S/N) continuum images to derive the stellar mass profiles.

We are currently studying the dynamics of the outflows in these QSO2s, which will address this issue in more detail (Trindade Falcão et al., in preparation).

6 CONCLUSIONS

We use long-slit spectroscopy, [O III] imaging, and CLOUDY photoionization models to determine the mass outflow rates and energetics as functions of distance from the nucleus in a sample of 12 nearby ($z < 0.12$) luminous ($L_{bol} > 1.6 \times 10^{45}$ erg s^{-1}) QSO2s. Our results are as follows:

(1) The outflows contain a total ionized gas mass ranging from $4.6^{+13.8}_{-3.4} \times 10^3 M_\odot$, for B2 1435+30, to $3.4^{+10.2}_{-2.5} \times 10^7 M_\odot$, for Mrk 34, with a total kinetic energy varying between $8.9^{+26.7}_{-6.7} \times 10^{50}$ erg, for SDSS J115245.66+101623.8, and $2.9^{+9.0}_{-2.2} \times 10^{55}$ erg, for Mrk 34.

(2) F2018 found that the outflows extend to a maximum of 1600 pc. Our results show that these outflows reach a peak outflow rate ranging from $\dot{M}_{out}(r) = 9.3^{+27.9}_{-7.0} \times 10^{-3}$ M$_\odot$ yr^{-1}, for B2 1435+30, to $10.3^{+30.9}_{-7.7}$ M$_\odot$ yr^{-1}, for Mrk 34, at distances between 100 and 1260 pc from the SMBH.

(3) The maximum kinetic luminosity of the outflow ranges from $3.4^{+10.2}_{-2.5} \times 10^{-8}$ of the AGN bolometric luminosity for SDSS J115245.66+101623.8 to $4.9^{+14.7}_{-3.7} \times 10^{-4}$ of the AGN bolometric luminosity for Mrk 34.[8] The large range in kinetic luminosity compared to the narrow range in L_{bol} (see Table 2) is in contrast to the correlation between the kinetic luminosity and L_{bol} suggested by Fiore et al. (2017). Our results indicate that the [O III] winds are not an efficient feedback mechanism, based on the criteria of Di Matteo et al. (2005) and Hopkins & Elvis (2010). This means that not only do the outflows not extend far enough to clear the bulge of gas (F2018), but also they lack the power to do so.

(4) As noted above, Mrk 34 is the target in our sample that shows the highest outflow rate and most extended outflows. We calculate what the outflow rates would have had to have been in order to reach the minimum value required for efficient feedback. We find that Mrk 34 would have to have, at its position of maximum $\dot{E}$, an outflow

---

[8]Our maximum kinetic luminosity value for Mrk 34 is about a factor of 10 less than that computed by Revalski et al. (2018). The discrepancy is due to the presence of a high-mass/low-density component, which was not included in our analysis.

rate of $20\,\mathrm{M_\odot\,yr^{-1}}$, corresponding to a mass of $8.2 \times 10^5\,\mathrm{M_\odot}$ at that position. This value is 10 times greater than our measured outflow rate at that same position. We also find that the required mass for efficient feedback is $\sim$0.01 times the amount for a covering factor of unity.

These calculations show that this object could potentially, at these velocities, make efficient outflows, but such energetic outflows are not detected. One possibility is that the lack of [O III] gas is the result of rapid thermal expansion, with the result that its ionization state increases to the point where it becomes X-ray-emitting gas. In fact, *Chandra* imaging of Mrk 34 has revealed X-ray emission-line gas extending the size of the [O III]-emission-line region (Fischer et al., in preparation). We are currently exploring this possibility (Trindade Falcão et al., in preparation). Also, neutral and molecular gas could be contributing to the outflow (see Section 2.5) and, altogether could provide a much higher mass outflow rate (Tombesi et al. 2015; Bischetti et al. 2019).

(5) Three of the targets in our sample show very extended [O III] emission, but weak outflow rates. Based on their compact outflow regions, but extended [O III] emission, we study two different scenarios: These AGNs were in a very low state until recently, but have entered a high state, during which they are able to accelerate outflows. Or these AGNs could be housed in more massive host galaxies, prohibiting successful radiative driving at distances greater than a few hundred parsec.

Based on these results, we do not see the outflows traced by [O III]-emission-line gas being powerful enough to generate efficient feedback. However, the presence of disturbed gas at larger radial distances (F2018) suggests that the AGNs have an effect outside the outflow regions. One possibility is that this is the result of X-ray winds, which may form from thermal expansion of the [O III] gas (Fischer et al. 2019; Kraemer et al. 2020). We are currently exploring this scenario (Trindade Falcão et al., in preparation).

DATA AVAILABILITY

Based on observations made with the NASA/ESA *HST*, and available from the Hubble Legacy Archive, which is a collaboration between the Space Telescope Science Institute (STScI/NASA), the Space Telescope European Coordinating Facility (ST-ECF/ESAC/ESA), and the Canadian Astronomy Data Centre (CADC/NRC/CSA).

REFERENCES

Ahumada R., Prieto C. A., Almeida A., Anders F., Anderson S. F., Andrews B. H., Anguiano B., 2020, 249, 3
Antonucci R., 1993, ARA&A, 31, 473
Bae H.-J., Woo J.-H., 2016, ApJ, 828, 97
Baron D., Netzer H., 2019, MNRAS, 482, 3915
Begelman M. C., 2004, Carnegie Obs. Astrophys. Ser., 1, 374
Bischetti M. et al., 2019, A&A, 628, A118
Buchner J. et al., 2014, A&A, 564, A125
Cardelli J. A., Clayton G. C., Mathis J. S., 1989, ApJ, 345, 245
Collins N. R., Collins S. B., Crenshaw D. M., Ruiz J., Deo R., Bruhweiler F. C., 2005, ApJ, 619, 116
Costa T., Sijacki D., Haehnelt M. G., 2014, MNRAS, 444, 2355
Crenshaw D. M., Kraemer S. B., 2005, ApJ, 625, 680
Crenshaw D. M., Kraemer S. B., 2012, ApJ, 753, 75
Crenshaw D. M., Kraemer S. B., George I. M., 2003, ARA&A, 41, 117
Crenshaw D. M., Kraemer S. B., Schmitt H. R., Jaffé Y. L., Deo R. P., Collins N. R., Fischer T. C., 2010, AJ, 139, 871
Crenshaw D. M., Fischer T. C., Kraemer S. B., Schmitt H. R., 2015, ApJ, 799, 83
Das V., Crenshaw D. M., Kraemer S. B., 2007, ApJ, 656, 699
Davies R. et al., 2020, MNRAS, 498, 4150
Di Matteo T., Springel V., Hernquist L., 2005, Nature, 433, 604
Dietrich M., Hamann F., Shields J. C., Constantin A., Heidt J., Jäger K., Vestergaard M., Wagner S. J., 2003, ApJ, 589, 722
Dong X., Wang T., Wang J., Yuan W., Zhou H., Dai H., Zhang K., 2008, MNRAS, 383, 581
Duras F. et al., 2020, A&A, 636, A73
Ferland G. J. et al., 2017, RMxAA, 49, 1379
Feroz F., Hobson M. P., 2008, MNRAS, 384, 449
Feroz F., Hobson M. P., Bridges M., 2009, MNRAS, 398, 1601
Feroz F., Hobson M. P., Cameron E., Pettitt A. N., 2013, Open J. Astrophys., 2
Fiore F. et al., 2017, A&A, 601, A143
Fischer T. C., Crenshaw D. M., Kraemer S. B., Schmitt H. R., 2013, ApJ, 209, 1
Fischer T. C., Crenshaw D. M., Kraemer S. B., Schmitt H. R., Turner T. J., 2014, ApJ, 785, 25
Fischer T. C. et al., 2017, ApJ, 834, 30
Fischer T. C. et al., 2018, ApJ, 856, 102
Fischer T. C. et al., 2019, ApJ, 887, 200
Gandhi P. et al., 2014, ApJ, 792, 117
Ganguly R., Brotherton M. S., 2008, ApJ, 672, 102
Genzel R. et al., 2014, ApJ, 796, 7
Greene J. E., Zakamska N. L., Ho L. C., Barth A. J., 2011, ApJ, 732, 9
Groves B. A., Dopita M. A., Sutherland R. S., 2004, A&AS, 153, 9
Hamann F., Ferland G., 1998, ARA&A, 37, 487
Harrison C. M., Alexander D. M., Mullaney J. R., Swinbank A. M., 2014, MNRAS, 441, 3306
Heckman T. M., Kauffmann G., Brinchmann J., Charlot S., Tremonti C., White S. D. M., 2004, ApJ, 613, 109
Hopkins P. F., Elvis M., 2010, MNRAS, 401, 7
Joye W. A., Mandel E., 2003, in Payne H.E., Jedrzejewski R.I., Hook R.N., eds, ASP Conf. Ser. Vol. 295, Astronomical Data Analysis Software and Systems XII, Astron. Soc. Pac., San Francisco, p. 489
King A., Pounds K., 2015, ARA&A, 53, 115
Kormendy J., Ho L. C., 2013, ARA&A, 51, 511
Kraemer S. B., Harrington J. P., 1986, ApJ, 307, 478

Kraemer S. B., Ruiz J. R., Crenshaw D. M., 1998, ApJ, 508, 232
Kraemer S. B., Crenshaw D. M., Hutchings J. B., Gull T. R., Kaiser M. E., Nelson C. H., Weistrop D., 2000, ApJ, 531, 278
Kraemer S. B. et al., 2001, ApJ, 551, 671
Kraemer S., Crenshaw D. M., George I. M., Netzer H., Turner T. J., Gabel J. R., 2002, ApJ, 577, 98
Kraemer S. B. et al., 2012, ApJ, 751, 84
Kraemer S. B., Turner T. J., Couto J. D., Crenshaw D. M., Schmitt H. R., Revalski M., Fischer T. C., 2020, MNRAS, 493, 3893
Lamastra A., Bianchi S., Matt G., Perola G. C., Barcons X., Carrera F. J., 2009, A&A, 504, 73
Laor A., Fiore F., Elvis M., Wilkes B. J., McDowell J. C., 1997, ApJ, 477, 93
Liu G., Zakamska N. L., Greene J. E., Nesvadba N. P. H., Liu X., 2013, ApJ, 436, 2576
McElroy R., Croom S. M., Pracy M., Sharp R., Ho I.-T., Medling A. M., 2015, MNRAS, 446, 2186
Mahoro A., Povic M., Nkundabakura P., 2017, MNRAS, 471, 3226
Meléndez M., Kraemer S. B., Weaver K. A., Mushotzky R. F., 2011, ApJ, 738, 6
Mullaney J. R., Alexander D. M., Fine S., Goulding A. D., Harrison C. M. C. H. R., 2013, MNRAS, 433, 622
Müller-Sánchez F., Prieto M. A., Hicks E. K. S., Vives-Arias H., Davies R. I., Malkan M., Tacconi L. J., Genzel R., 2011, ApJ, 739, 69
Nagao T., Murayama T., Taniguchi Y., 2001, ApJ, 546, 744
Nagao T., Murayama T., Shioya Y., Taniguchi Y., 2002, ApJ, 575, 721
Nahar S. N., 1999, ApJS, 120, 131
Netzer H., 2009, MNRAS, 399, 1907
Netzer H., Chelouche D., George I. M., Turner T. J., Crenshaw D. M., Kraemer S., Nandra K., 2002, ApJ, 571, 256
Nevin R., Comerford J., Müller-Sánchez F., Barrows R., Cooper M., 2016, ApJ, 832, 67
Osterbrock D. E., Ferland G. J., 2006, Astrophysics of Gaseous Nebulae and Active Galactic Nuclei, 2nd edn. Univ. Sci. Books, Sausalito, CA, USA

Peterson B. M., 1997, An Introduction to Active Galactic Nuclei, 16th edn. Cambridge Univ. Press, Cambridge, NY, USA
Rafter S. E., Crenshaw D. M., Wiita P. J., 2009, AJ, 137, 42
Revalski M. et al., 2018, ApJ, 867, 88
Reyes R. et al., 2008, AJ, 136, 2373
Ryon J. E., 2019, ACS Instrument Handbook, Version 18.0 edn. STScI, Baltimore
Savage B. D., Mathis J. S., 1979, ARA&A, 17, 73
Seaton M. J., 1979, MNRAS, 187, 73
Silk J., 2013, ApJ, 722, 112
Snow T. P., Witt A. N., 1996, ApJ, 468, L65
Storchi-Bergmann T., Schnorr-Muller A., 2019, Nat. Astron., 3, 48
Storchi-Bergmann T., Rodríguez-Ardila A., Schmitt H. R., 1996, AJ, 472, 83
Storchi-Bergmann T., Schmitt H. R., Calzetti D., Kinney A. L., 1998, AJ, 115, 909
Talbot R. J. J., Arnett W. D., 1973, ApJ, 186, 51
Tombesi F., Meléndez M., Veilleux S., Reeves J. N., González-Alfonso E., Reynolds C. S., 2015, Nature, 519, 436
Veilleux S., Cecil G., Bland-Hawthorn J., 2005, ARA&A, 43, 769
Woodgate B. E., Kimble R. A., Bowers C. W., Kraemer S., Kaiser M. E., Danks A. C., Grady J. F., Loiacono J. J., 1998, Astron. Soc. Pac., 110, 1183
Woo J.-H., Bae H.-J., Son D., Karouzos M., 2016, ApJ, 817, 108
Wylezalek D., Morganti R., 2018, Nat. Astron., 2, 181
Wylezalek D., Zakamska N. L., 2016, MNRAS, 461, 3724
Zubovas K., Bourne M. A., 2017, MNRAS, 468, 4956
Zubovas K., King A., 2012, in Chartas G., Hamann F., Leighly K. M., eds, AGN Winds in Charleston, Astronomic Society of the Pacific Series, 460. Charleston, South Carolina, p. 235
Zakamska 2003, The Astronomical Journal, 2125, 0004

This paper has been typeset from a TeX/LaTeX file prepared by the author.